A Comprehensive Segmentation, Registration, and Cancer Detection Scheme on 3 Tesla *In Vivo* Prostate DCE-MRI

Satish Viswanath[1], B. Nicolas Bloch[2], Elisabeth Genega[2], Neil Rofsky[2], Robert Lenkinski[2], Jonathan Chappelow[1], Robert Toth[1], and Anant Madabhushi[1]

[1] Department of Biomedical Engineering, Rutgers University, NJ, USA
anantm@rci.rutgers.edu
[2] Department of Radiology, Beth Israel Deaconess Medical Center, MA, USA*

Abstract. Recently, high resolution 3 Tesla (T) Dynamic Contrast-Enhanced MRI (DCE-MRI) of the prostate has emerged as a promising modality for detecting prostate cancer (CaP). Computer-aided diagnosis (CAD) schemes for DCE-MRI data have thus far been primarily developed for breast cancer and typically involve model fitting of dynamic intensity changes as a function of contrast agent uptake by the lesion. Comparatively there is relatively little work in developing CAD schemes for prostate DCE-MRI. In this paper, we present a novel unsupervised detection scheme for CaP from 3 T DCE-MRI which comprises 3 distinct steps. First, a multi-attribute active shape model is used to automatically segment the prostate boundary from 3 T *in vivo* MR imagery. A robust multimodal registration scheme is then used to non-linearly align corresponding whole mount histological and DCE-MRI sections from prostatectomy specimens to determine the spatial extent of CaP. Non-linear dimensionality reduction schemes such as locally linear embedding (LLE) have been previously shown to be useful in projecting such high dimensional biomedical data into a lower dimensional subspace while preserving the non-linear geometry of the data manifold. DCE-MRI data is embedded via LLE and then classified via unsupervised consensus clustering to identify distinct classes. Quantitative evaluation on 21 histology-MRI slice pairs against registered CaP ground truth estimates yielded a maximum CaP detection accuracy of 77.20% while the popular three time point (3TP) scheme yielded an accuracy of 67.37%.

1 Introduction

Prostatic adenocarcinoma (CaP) is the second leading cause of cancer related deaths among males in the United States, with an estimated 186,000 new cases

* This work is made possible via grants from the Wallace H. Coulter Foundation, New Jersey Commission on Cancer Research, National Cancer Institute (R21CA127186-01,R03CA128081-01), the Department of Defense, and the Society for Imaging Informatics in Medicine (SIIM).

D. Metaxas et al. (Eds.): MICCAI 2008, Part I, LNCS 5241, pp. 662–669, 2008.

in 2008 (Source: *American Cancer Society*). Recently, high resolution 3 Tesla (T) endorectal *in vivo* prostate Dynamic Contrast-Enhanced MRI (DCE-MRI) has been shown to discriminate effectively between normal and cancerous regions [1].

Most current efforts in computer-aided diagnosis of CaP from DCE-MRI involve pharmacokinetic curve fitting such as in the 3 Time Point (3TP) scheme [2]. Based on the curve/model fits these schemes attempt to identify wash-in and wash-out points, i.e. time points at which the lesion begins to take up and flush out the contrast agent. Lesions are then identified as benign, malignant or indeterminate based on the rate of the contrast agent uptake and wash out. Vos et al. [3] described a supervised CAD scheme for analysis of the peripheral zone of the prostate. Pharmacokinetic features derived from curve fitting were used to train the model and coarse quantitative evaluation was performed based on a roughly registered spatial map of CaP on MRI. Area under the Receiver Operating Characteristic (ROC) curve (AUC) was used as a measure of accuracy. A mean AUC of 0.83 was reported. Due to the lack of perfect slice correspondences between MRI and histology data and the large difference in the number of slices between the two modalities, we suggest training a supervised classification system based on such labels would be inappropriate.

The 3TP and pharmacokinetic modeling approaches assume linear changes in the dynamic MR image intensity profiles. We have previously shown that such data suffers from intensity non-standardness [4] wherein MR image intensities do not have fixed tissue-specific meaning within the same imaging protocol, body region, and patient. Figures 1(a), (b), and (c) show the image intensity histograms for the non-lesion areas within 7 3 T *in vivo* DCE-MRI prostate studies for timepoints $t = 2$, $t = 4$, and $t = 6$ respectively. An obvious intensity drift in the MR images can be seen in the apparent mis-alignment of the intensity histograms. Non-linear dimensionality reduction methods such as locally linear embedding (LLE) [5] have been shown to faithfully preserve relative object relationships in biomedical data from the high- to the low-dimensional representation. Varini et al. [6] performed an exploratory analysis of breast DCE-MRI data via different dimensionality reduction methods. LLE was found to be more robust and accurate in differentiating between benign and malignant tissue classes as compared to linear methods such as Principal Component Analysis (PCA).

In this paper we present a comprehensive segmentation, registration and detection scheme for CaP from 3 T *in vivo* DCE-MR imagery that has the following main features: (1) a multi-attribute active shape model [7] is used to automatically segment the prostate boundary, (2) a multimodal non-rigid registration scheme [8] is used to map CaP extent from whole mount histological sections onto corresponding DCE-MR imagery, and (3) an unsupervised CaP detection scheme involving LLE on the temporal intensity profiles at every pixel location followed by classification via consensus clustering [9]. Our proposed methodology is evaluated on a per-pixel basis against registered spatial maps of CaP on MRI. Additionally, we quantitatively compare our results with those obtained from the 3TP method for a total of 21 histology-MRI slice pairs.

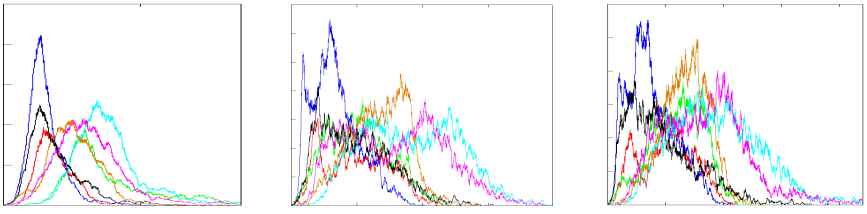

(a) (b) (c)

Fig. 1. Image intensity histograms for non-cancerous regions in 7 *in vivo* 3 T DCE-MRI prostate studies at time points (a) $t = 2$, (b) $t = 4$, and (c) $t = 6$. A very obvious misalignment between the MR intensity histograms across the 7 DCE-MRI studies is apparent at multiple time points.

2 Experimental Design

2.1 Data Description and Notation

A total of 21 3 T *in vivo* endorectal MR (T2-weighted and DCE protocols) images with corresponding whole mount histological sections (WMHS) following radical prostatectomy were obtained from 6 patient datasets from the Beth Israel Deaconess Medical Center. The DCE-MR images were acquired during and after a bolus injection of 0.1 mmol/kg of body weight of gadopentetate dimeglumine using a 3-dimensional gradient echo sequence (3D-GE) with a temporal resolution of 1 min 35 sec. Following radical prostatectomy, whole-mount sections of the prostate were stained via Haemotoxylin and Eosin (H & E) and examined by a trained pathologist to accurately delineate the presence and extent of CaP.

We define a 2D DCE-MR image $\mathcal{C}^{D,t} = (C, f^{D,t})$ where C is a set of spatial locations $c_i \in C, i \in \{1, \ldots, |C|\}$, $|C|$ is the cardinality of C and $t \in \{1, \ldots, 7\}$. $f^{D,t}(c)$ then represents the intensity value at location $c \in C$ at timepoint t. We define a 2D T2-weighted (T2-w) MR image as $\mathcal{C}^{T_2} = (C, f^{T_2})$ and the corresponding WMHS as $\mathcal{C}^H$. $G(\mathcal{C}^H)$ is defined as the set of locations in the WMHS $\mathcal{C}^H$ that form the spatial extent of CaP ("gold standard").

2.2 Automated Boundary Segmentation on *in vivo* MR Imagery

We have recently developed a Multi-Attribute, Non-initializing, Texture Reconstruction based Active shape model (MANTRA) [7] algorithm. Unlike traditional ASMs, MANTRA makes use of local texture model reconstruction to overcome limitations of image intensity, as well as multiple attributes with a combined mutual information metric. MANTRA also requires only a rough initialization (such as a bounding-box) around the prostate to be able to segment the boundary accurately.

Step 1 (Training): PCA is performed on expert selected landmarks along the prostate border to generate a statistical shape model. A statistical texture model

is calculated for each landmark point by performing PCA across patches of pixels sampled from areas surrounding each landmark point in each training image.

Step 2 (Segmentation): Regions within a new image are searched for the prostate border and potential locations have patches of pixels sampled from around them. The pixel intensity values within a patch are reconstructed from the texture model as best possible, and mutual information is maximized between the reconstruction and the original patch to test for a border location. An active shape model (ASM) is fit to such locations, and the process repeats until convergence. Figure 2(a) shows an original sample T2-w image $\mathcal{C}^{T_2}$. The final segmentation of the prostate boundary via MANTRA is seen in Figure 2(b) in green. MANTRA is applied to segment the prostate boundary for all images $\mathcal{C}^{T_2}$ and $\mathcal{C}^{D,t}, t \in \{1, \ldots, 7\}$.

2.3 Establishment of CaP Ground Truth on DCE-MRI Via Elastic Multimodal Registration of Histology, T2-w, and DCE-MRI

This task comprises the following steps:

1. Affine alignment of $\mathcal{C}^H$ to corresponding $\mathcal{C}^{T_2}$ is done using our Combined Feature Ensemble Mutual Information (COFEMI) scheme, previously presented in [8]. This is followed by elastic registration using thin plate splines (TPS) warping based of $\mathcal{C}^H$ (Figure 2(c)) to correct for non-linear deformations from endorectal coil in $\mathcal{C}^{T_2}$ (Figure 2(b)) and histological processing.
2. Having placed $\mathcal{C}^{T_2}$ and $\mathcal{C}^H$ in spatial correspondence, the histological CaP extent $G(\mathcal{C}^H)$ is mapped onto $\mathcal{C}^{T_2}$ to obtain $G^r(\mathcal{C}^{T_2})$ via the transformation r determined in step 1.
3. MI-based affine registration of $\mathcal{C}^{T_2}$ to $\mathcal{C}^{D,5}$ (chosen due to improved contrast) is done to correct for subtle misalignment and resolution mismatch between the MR protocols. It is known that the individual DCE time point images $\mathcal{C}^{D,t}, t \in \{1, \ldots, 7\}$ are in implicit registration, hence requiring no alignment.
4. Mapping of histology-derived CaP ground truth $G^r(\mathcal{C}^{T_2})$ (Figure 2(d)) onto $\mathcal{C}^{D,5}$ to obtain $G^R(\mathcal{C}^{D,5})$ via the transformation R determined in step 3.

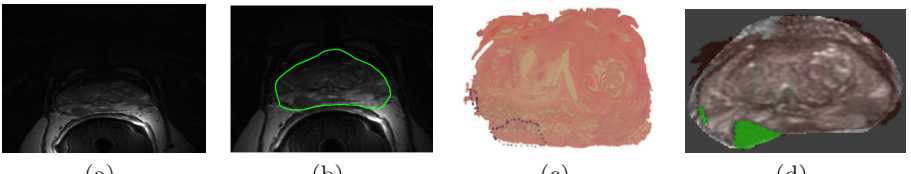

(a) (b) (c) (d)

Fig. 2. (a) Original 3 T *in vivo* endorectal T2-w prostate MR image $\mathcal{C}^{T_2}$, (b) prostate boundary segmentation via MANTRA in green, (c) corresponding WMHS $\mathcal{C}^H$ with CaP extent $G(\mathcal{C}^H)$ outlined in blue by a pathologist, (d) result of registration of $\mathcal{C}^H$ and $\mathcal{C}^{T_2}$ via COFEMI visualized by an overlay of $\mathcal{C}^H$ onto $\mathcal{C}^{T_2}$. The mapped CaP extent $G^r(\mathcal{C}^{T_2})$ is highlighted in green.

2.4 Classification of DCE-MRI Via LLE and Consensus Clustering

Locally Linear Embedding (LLE): For each pixel c within each DCE-MR image $\mathcal{C}^{D,t}, t \in \{1,\ldots,7\}$, there is an associated intensity feature vector $F(c_i) = [f^{D,t}(c_i)|t \in \{1,\ldots,7\}], c_i \in C, i \in \{1,\ldots,|C|\}$. LLE [5] is used to embed the set $\mathcal{F} = \{F(c_1), F(c_2), \ldots, F(c_p)\}$, $p = |C|$ to result in the set of lower dimensional embedding vectors $\mathcal{X} = \{X_{LLE}(c_1), X_{LLE}(c_2), \ldots, X_{LLE}(c_p)\}$. Let $\{c_{\eta_i(1)}, \ldots, c_{\eta_i(m)}\}$ be the m nearest neighbors (mNN) of c_i where $\eta_i(m)$ is the index of the m^{th} neighbor of $c_i \in C$. $F(c_i)$ is then approximated by a weighted sum of its own mNN, $F\left(c_{\eta_i(1)}\right)$,$F\left(c_{\eta_i(2)}\right)$,...,$F\left(c_{\eta_i(m)}\right)$ by assuming local linearity, thus allowing us to use Euclidean distances between the neighbors. The optimal reconstruction weights are given by the sparse matrix $W_{LLE} \in \Re^{|C|\times|C|}$:

$$\psi_1(W_{LLE}) = \sum_{i=1}^{p} \left\| F(c_i) - \sum_{j=1}^{m} W_{LLE}(i,\eta_i(j)) F\left(c_{\eta_i(j)}\right) \right\|_2, \tag{1}$$

subject to the constraints $W_{LLE}(i,j) = 0$ if c_j does not belong to the mNN of c_i and $\sum_j W_{LLE}(i,j) = 1, c_i, c_j \in C$. The low-dimensional projection of the points in $\mathcal{F}$ that preserves the weighting in W_{LLE} is determined by approximating each projection $X_{LLE}(c_i)$ as a weighted combination of its own mNN. The optimal $\mathcal{X}_{LLE}$ in the least squares sense minimizes

$$\psi_2(\mathcal{X}_{LLE}) = \sum_{i=1}^{p} \left\| X_{LLE}(c_i) - \sum_{j=1}^{p} W_{LLE}(i,j) X_{LLE}(c_j) \right\|_2 = \text{tr}\left(\mathcal{X}_{LLE} L \mathcal{X}_{LLE}^{\mathsf{T}}\right), \tag{2}$$

where tr is the trace operator, $\mathcal{X}_{LLE} = [X_{LLE}(c_1), X_{LLE}(c_2), \ldots, X_{LLE}(c_p)]$, $L = (I - W_{LLE})\left(I - W_{LLE}^{\mathsf{T}}\right)$ and I is the identity matrix. The minimization of (2) subject to the constraint $\mathcal{X}_{LLE}\mathcal{X}_{LLE}^{\mathsf{T}} = I$ (a normalization constraint that prevents the solution $\mathcal{X}_{LLE} \equiv \mathbf{0}$) is an Eigenvalue problem whose solutions are the Eigenvectors of the Laplacian matrix L.

Unsupervised classification via consensus *k*-means clustering: To overcome the instability associated with centroid based clustering algorithms, we generate N weak clusterings $\tilde{V}_n^1, \tilde{V}_n^2, \ldots, \tilde{V}_n^k, n \in \{0,\ldots,N\}$ by repeated application of k-means clustering for different values of $k \in \{3,\ldots,7\}$ on the low dimensional manifold $X_{LLE}(c)$, for all $c \in C$, and combine them via consensus clustering [9]. As we do not know *a priori* the number of classes (clusters) to look for in the data, we vary k to determine upto 7 possible classes in the data. A co-association matrix H is calculated with the underlying assumption that pixels belonging to a *natural* cluster are very likely to be co-located in the same cluster for each iteration. $H(i,j)$ thus represents the number of times $c_i, c_j \in C, i \neq j$ were found in the same cluster $\tilde{V}_n^k$ over N iterations. If $H(i,j) = N$ then there is a high likelihood that c_i, c_j do indeed belong to the same cluster. We apply multidimensional scaling [10] (MDS) to H, which finds optimal positions for the data points c_i, c_j in lower-dimensional space through minimization of the least

squares error in the input pairwise similarites in H. A final unsupervised classification via k-means is used to obtain the stable clusters $V_k^1, V_k^2, \ldots, V_k^q, q = k$ for all $k \in \{3, \ldots, 7\}$.

3 Results

3.1 Qualitative Results

Representative results from experiments on 21 DCE-histology slice pairs are shown in Figure 3 with each row corresponding to a different dataset. Corresponding histology sections (not shown) were registered to DCE-MRI data ($\mathcal{C}^{D,5}$) to obtain the ground truth estimate $G^R(\mathcal{C}^{D,5})$ shown in Figures 3(a), 3(e), and 3(i) highlighted in green. Figures 3(b), 3(f) and 3(j) show the RGB scaled values of $X_{LLE}(c)$ at every $c \in C$ by representing every spatial location on the image by its embedding co-ordinates and scaling these values to display as an RGB image. Similar colors in Figures 3(b), 3(f) and 3(j) represent pixels embedded close together in the LLE-reduced space. Each of the clusters $V_k^1, V_k^2, \ldots, V_k^q$ for each value of $k \in \{3, \ldots, 7\}$ are evaluated against $G^R(\mathcal{C}^{D,5})$ and the cluster showing the most overlap is considered to be the cancer class. Figures 3(c), 3(g), and 3(k) show the result of plotting this cluster back onto the slice (in red). Figures 3(d), 3(h) and 3(l) show 3TP results based on the DCE images $\mathcal{C}^{D,t}, t \in \{1, \ldots, 7\}$ in Figures 3(a), 3(e), and 3(i). Red, blue and green colors are used to represent different classes based on the ratio $w = \frac{\text{Rate of wash-in}}{\text{Rate of wash-out}}$ of the contrast agent uptake. When w is close to 1, the corresponding pixel is identified as cancerous area (red), when w is close to zero, the pixel is identified as benign (blue), and green pixels are those are identified as indeterminate.

3.2 Quantitative Evaluation against Registered CaP Ground Truth Estimates on DCE

For each of 21 slices, labels corresponding to the clusters $V_k^1, V_k^2, \ldots, V_k^q, q = k$, for each $k \in \{3, 4, 5, 6, 7\}$ are each evaluated against the registered CaP extent on DCE-MRI ($G^R(\mathcal{C}^{D,5})$). The cluster label showing the largest overlap with this ground truth is then chosen as the cancer class. This class is used to calculate the sensitivity, specificity, and accuracy of our CAD system at a particular k value for the slice under consideration. These values are then averaged across all 21 slices and are summarized in Table 1. The maximum sensitivity observed is 60.64% ($k = 3$), the maximum specificity is 84.54% ($k = 7$), and the maximum accuracy is 77.20%($k = 7$). We see a reduction in sensitivity as k increases from 3 to 7, with a corresponding increase in specificity and accuracy. Using the 3TP technique (which assumes that only 3 classes can exist in the data), we achieve a sensitivity of 41.53% and sensitivity of 70.04%. It can be seen that our proposed technique has an improved performance as compared to the popular state-of-the-art 3TP method across $k \in \{3, 4, 5, 6, 7\}$.

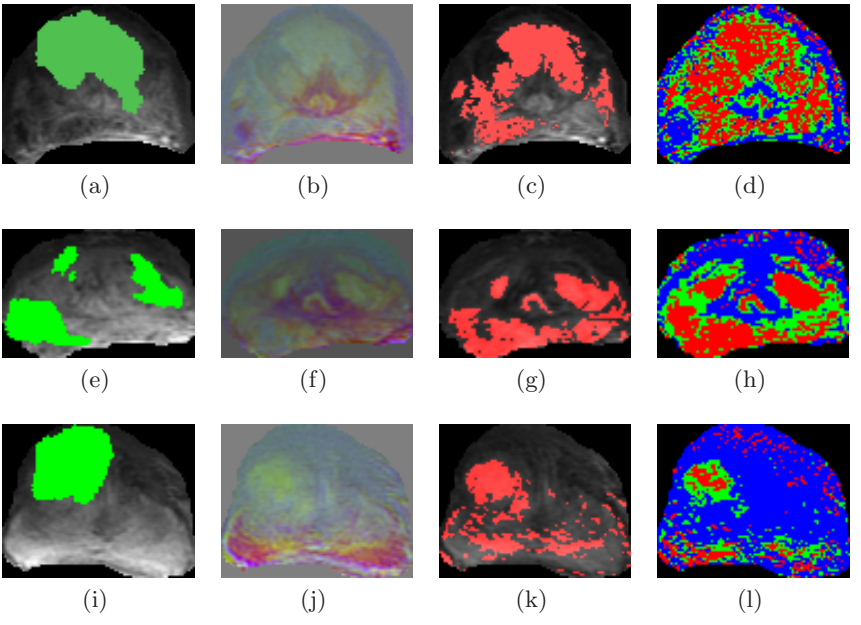

Fig. 3. (a), (e), (i) showing the CaP extent $G^R(\mathcal{C}^{D,5})$ on the DCE-MRI slice $\mathcal{C}^{D,5}$ highlighted in green via registration with corresponding histology (not shown), (b), (f), (j) RGB visualization of the embedding coordinates from X_{LLE} onto the slice, (c), (g), (k) classification result from plotting the cluster in $V_k^1, V_k^2, \ldots, V_k^q, q = k$ (for $k = 3$) that shows the highest overlap with the ground truth $G^R(\mathcal{C}^{D,5})$ back onto the slice in red, (d), (h), (l) results from using the 3TP method on the DCE data. The improved correspondence of the red regions in (c), (g), (k) with the ground truth over the red regions in the 3TP results in (d), (h), (l) can be seen.

Table 1. CaP detection sensitivity and specificity at the pixel resolution averaged over 21 3 T DCE-MRI datasets. These are compared for different values of k within consensus clustering, as well as for the 3TP method.

	k=3	k=4	k=5	k=6	k=7	3TP
Sensitivity	60.64	51.77	49.06	42.33	41.73	41.53
Specificity	65.80	76.24	79.60	83.30	84.54	70.04
Accuracy	64.54	71.30	74.20	76.65	77.20	67.37

Comparison against existing prostate DCE CAD: Analyzing the results by Vos et al. [3] in differentiating between non-malignant suspicious enhancing and malignant lesions in the prostate, reveal that their sensitivity of 83% corresponds to a 58% specificity. These values were obtained by only considering the peripheral zone of the prostate. Comparatively our metrics (60.64% sensitivity, 84.54% specificity, and 77.20% accuracy) have been achieved when examining the *whole* of the prostate while utilizing a more rigorously registered CaP extent for evaluation. We may hypothesize that had we similarly limited our analysis

to the peripheral zone alone, our results would have been markedly superior compared to those reported in [3].

4 Concluding Remarks

In this paper we have presented a novel comprehensive methodology for segmentation, registration, and detection of prostate cancer from 3 Tesla *in vivo* DCE prostate MR images. A multi-attribute active shape model based segmentation scheme (MANTRA) was used to automatically segment the prostate from *in vivo* DCE and T2-w images, following which a multimodal registration algorithm, COFEMI, was used to map spatial extent of CaP from corresponding whole mount histology to the DCE-MRI slices. Owing to the presence of MR image intensity non-standardness we utilized a non-linear DR scheme (LLE) coupled with consensus clustering to identify cancerous image pixels. Our CaP detection results, 60.72% sensitivity, 83.24% specificity, and 77.20% accuracy compare very favourably with results obtained by Vos et al [3] and were superior compared to those obtained via the 3TP method (41.53% sensitivity, 70.04% specificity, 67.37% accuracy). Future work will focus on validating our methodology on a much larger cohort of data.

References

1. Padhani, A., Gapinski, C., et al.: Dynamic Contrast Enhanced MRI of Prostate Cancer: Correlation with Morphology and Tumour Stage, Histological Grade and PSA. Clinical Radiology 55(2), 99–109 (2000)
2. Degani, H., Gusis, V., et al.: Mapping pathophysiological features of breast tumours by MRI at high spatial resolution. Nature Medicine 3(7), 780–782 (1997)
3. Vos, P., Hambrock, T., et al.: Computerized analysis of prostate lesions in the peripheral zone using dynamic contrast enhanced MRI. Medical Physics 35(3), 888–899 (2008)
4. Madabhushi, A., Udupa, J.: New Methods of MR Image Intensity Standardization via Generalized Scale. Medical Physics 33(9), 3426–3434 (2006)
5. Roweis, S., Saul, L.: Nonlinear Dimensionality Reduction by Locally Linear Embedding. Science 290(5500), 2323–2326 (2000)
6. Varini, C., Degenhard, A., et al.: Visual exploratory analysis of DCE-MRI data in breast cancer by dimensional data reduction: a comparative study. Biomedical Signal Processing and Control 1(1), 56–63 (2006)
7. Toth, R., Tiwari, P., et al.: A multi-modal prostate segmentation scheme by combining spectral clustering and active shape models. In: SPIE Medical Imaging, pp. 69144S1–69144S12 (2008)
8. Chappelow, J., Madabhushi, A., et al.: A combined feature ensemble based mutual information scheme for robust inter-modal, inter-protocol image registration. In: International Symposium on Biomedical Imaging, pp. 644–647 (2007)
9. Fred, A., Jain, A.: Combining Multiple Clusterings Using Evidence Accumulation. IEEE Transactions on Pattern Analysis and Machine Intelligence 27(6), 835–850 (2005)
10. Venna, J., Kaski, S.: Local multidimensional scaling. Neural Networks 19(6), 889–899 (2006)